An Assessment of the Skill of GEOS-5 Seasonal forecasts

Yoo-Geun Ham[1,2], Siegfried Schubert[1], and Michele M. Rienecker[1]

[1]Global Modeling and Assimilation Office, GSFC/NASA, Greenbelt, Maryland, USA,

[2]Goddard Earth Sciences Technology and Research Studies and Investigations, Morgan state university

September, 2013

Submitted to Climate Dynamics

Corresponding author address: Dr. Yoo-Geun Ham, NASA Goddard Space Flight Center, Code 610.1, Greenbelt, Maryland, USA.

E-mail: yoo-geun.ham@nasa.gov

Tel.: +1-301-614-6545

Fax: +1-301-614-6246

Abstract

The seasonal forecast skill of the NASA Global Modeling and Assimilation Office (GMAO) coupled global climate model (CGCM) is evaluated based on an ensemble of 9-month lead forecasts for the period 1993 to 2010. The results from the current version (V2) of the CGCM consisting of the GEOS-5 AGM coupled to the MOM4 ocean model are compared with those from an earlier version (V1) in which the AGCM (the NSIPP model) was coupled to the Poseidon Ocean Model. It was found that the correlation skill of the Sea Surface Temperature (SST) forecasts is generally better in V2, especially over the sub-tropical and tropical central and eastern Pacific, Atlantic, and Indian Ocean. Furthermore, the improvement in skill in V2 mainly comes from better forecasts of the developing phase of ENSO from boreal spring to summer. The skill of ENSO forecasts initiated during the boreal winter season, however, shows no improvement in terms of correlation skill, and is in fact slightly worse in terms of root mean square error (RMSE).

The degradation of skill is found to be due to an excessive ENSO amplitude. For V1, the ENSO amplitude is too strong in forecasts starting in boreal spring and summer, which causes large RMSE in the forecast. For V2, the ENSO

45 amplitude is slightly stronger than that in observations and V1 for forecasts
46 starting in boreal winter season. An analysis of the terms in the SST tendency
47 equation, shows that this is mainly due to an excessive zonal advective
48 feedback. In addition, V2 forecasts that are initiated during boreal winter
49 season, exhibit a slower phase transition of El Nino, which is consistent with
50 larger amplitude of ENSO after the ENSO peak season. It is found that this is
51 due to weak discharge of equatorial Warm Water Volume (WWV). In both
52 observations and V1, the discharge of equatorial WWV leads the equatorial
53 geostrophic easterly current so as to damp the El Nino starting in January. This
54 process is delayed by about 2 months in V2 due to the slower phase transition
55 of the equatorial zonal current from westerly to easterly.
56

1. Introduction

During the last few decades, dynamical forecast systems using coupled atmosphere-ocean GCMs (CGCMs) have produced significant improvements in seasonal forecast skill, particularly during times when El Nino Southern Oscillation (ENSO) is active. This progress is reflected in a number of operational or semi-operational dynamical seasonal forecast systems in various institutes around the world (e.g., Bacmeister et al. 2000; Wang et al. 2002; Palmer et al. 2004; Luo et al. 2005; Saha et al. 2006; Molteni et al. 2011; Ham et al. 2012a). In general, most current seasonal forecast systems exhibit successful prediction of ENSO at lead time ranging from two to four seasons, which beats the prediction skill using persistence or other more sophisticated statistical models. The improvements in skill appear to be the result of a combination of factors including more realistic model formulations (Luo et al. 2005; Yuan et al. 2011), improved initialization procedures (Rosati et al. 1997; Zhang et al. 2007; Keppenne et al 2008; Balmaseda and Anderson 2009; Yin et al. 2011), and the use of optimal initial perturbations for ensemble forecasting (Yang et al. 2006, 2008; Kug et al. 2011; Ham et al. 2009, 2012c).

In addition to the success of individual forecast systems, Multi-Model Ensemble (MME) prediction systems can lead to additional improvements in forecast skill, by reducing the uncertainties due to the model errors in

77 individual forecast systems (Yoo and Kang, 2005; Wang et al. 2009). The
78 positive impact of MME approaches is now well documented as a result of
79 several international projects including the European Multimodel Ensemble
80 System for Seasonal-to-Interannual Prediction (DEMETER) (Palmer et al. 2004),
81 the Asia–Pacific economic cooperation climate center (APCC)/climate
82 prediction and its application to society (CliPAS) project (Wang et al. 2009), and
83 the U.S. National Multi-Model Ensemble (NMME [1], http://www.cpc.ncep.noaa.gov/ products/NMME/) project.

85 The current version of the NASA GMAO seasonal forecast system
86 (CGCMv2: Vernieres et al. 2013; Ham et al. 2012c,d) consists of the GEOS-5
87 AGCM (Molod et al. 2012) coupled to the MOM4 ocean model (Griffies et al.
88 2005). This is a major update of an earlier forecast system (CGCMv1) consisting
89 of the NASA Seasonal-to-Interannual Prediction Project (NSIPP) AGCM
90 (Bacmeister et al. 2000) coupled to the Poseidon ocean model (Schopf and
91 Loughe 1995). Further details of the two forecast systems are provided in the
92 next section.

93 The aim of this study is to evaluate and compare the forecast skill of the two
94 versions of the NASA GMAO seasonal forecast systems. An important aspect

[1] The US National Multi-Model Ensemble (NMME) is an experimental multi-model seasonal forecasting system consisting of coupled models from NOAA/NCEP, NOAA/GFDL, IRI, NCAR, NASA, and Canada's CMC.

of the study is that we address the physical mechanisms responsible for any differences in the forecast skill between the two versions.

Section 2 describes the two GMAO seasonal forecast systems, the hindcast experiments, and the observations used in this study. In section 3, we compare the seasonal forecast skill of the two forecast systems. The physical mechanisms responsible for the differences in forecast skill between the two systems are discussed in section 4. The summary and discussion are given in section 5.

2. The GMAO seasonal forecast systems, and validating observations

a. The V1 forecast system

The CGCMv1 consists of the NASA Seasonal-to-Interannual Prediction Project atmospheric general circulation model (NSIPP AGCM) described in Bacmeister et al. (2000), the Poseidon ocean GCM (Schopf and Loughe 1995), and the Mosaic land surface model (Koster and Suarez 1992). The convective parameterization is the Relaxed Arakawa-Schubert (RAS) scheme (Moorthi and Suarez, 1992). The resolution of the NSIPP AGCM is 2.5 ^{o} longitude by 2^{o} latitude with 34 sigma vertical levels. The Poseidon OGCM is a reduced-gravity isopycnal model, with a resolution of 5/8 ^{o} longitude by 1/3^{o} latitude, and 27 vertical layers. The atmosphere and ocean is coupled daily without any flux

corrections.

The oceanic initial conditions are from an analysis that uses Optimal Interpolation to assimilate ocean temperature observations, while the atmospheric states are taken from AMIP-style simulations with the NSIPP AGCM – runs forced with observed sea surface temperatures (SSTs). The forecasts start at the 1st day of the month from 1993 to 2010. The six ensemble members used in this study have initial conditions that consist of the assimilated fields and 5 other states constructed by perturbing either the oceanic or atmospheric states.

b. The V2 forecast system

The NASA/GMAO GEOS-5 AOGCM consists of the GEOS-5 AGCM and the Modular Ocean Model version 4 (MOM4) (Griffies et al., 2005). The atmospheric component of the GEOS-5 model used here has 72 vertical levels and 2° latitude by 2.5° longitude grid spacing. The dynamic core is based on a finite volume method (Lin 2004). The convective parameterization is again the Relaxed Arakawa-Schubert (RAS) scheme (Moorthi and Suarez, 1992), though with substantial improvements (Molod et al. 2012). More details about the GEOS-5 atmospheric model are provided in Rienecker et al. (2007) and Molod et al. (2012). The ocean model uses a B-grid finite difference treatment of the

133 primitive equations of motion, Boussinesq and hydrostatic approximations in
134 spherical coordinates, and covers the global oceans with realistic coastlines and
135 bathymetry. The resolution is 50 vertical levels and a 1^{o}x1^{o} horizontal grid
136 telescoping to $1/3^{o}$ meridional spacing near the equator. The vertical grid
137 spacing is a constant 10 m over the top 225 m. Air–sea fluxes are exchanged at
138 every time step.

139 The initial conditions are obtained from an ocean assimilation employing
140 the GEOS-5 AOGCM and a multi-variate Ensemble Optimal Interpolation
141 (EnOI) analysis scheme that ingests various temperature and salinity
142 observations, while the atmosphere is constrained by MERRA (Rienecker et al.
143 2011). We utilize initial condition from assimilated states and 5 more ensemble
144 members from the perturbed initial conditions using the breeding and random
145 perturbation (i.e. total 6 ensemble members). The forecast period is 1981-2010,
146 but we only utilize the data from 1993 for the consistency with V1 forecast
147 period.

148 *c. Observational data*

149 The observed SST data are from the National Oceanic and Atmospheric
150 Administration (NOAA) Extended Reconstructed Sea Surface Temperatures
151 version 3 from NOAA/OAR/ESRL (ERSST V3b, http://www.esrl.noaa.gov/psd/).

152 The monthly-mean zonal wind stress data are from ERA Interim (Dee et al.
153 2011). The ocean temperature and current data are obtained from the NCEP
154 Global Ocean Data Assimilation system (GODAS, Behringer and Xue, 2004). For
155 precipitation, we use the Global Precipitation Climatology Project (GPCP)
156 monthly-mean precipitation data from WMO/WCRP/GEWEX (Adler et al. 2003).
157 The analyzed periods for all observations are from 1993 to 2010.

158

159 **3. Seasonal forecast skill**

160 We first compare the bias (i.e. the time mean ensemble-mean forecast minus
161 the time mean observed) in 3-month averaged Sea Surface Temperature (SST)
162 fields for 2 to 4 month lead times, for forecasts initiated at the beginning of
163 March, June, September, and December (Figure 1). In V1, the general spatial
164 pattern of the SST bias over the Pacific is similar regardless of the month the
165 forecasts were initiated. The cold bias is mainly over the western and equatorial
166 far-eastern Pacific, while there is positive SST bias of about 1.5^{o}C over the
167 southern far-eastern Pacific. The cold SST bias over the western Pacific is
168 relatively strong over the northern hemisphere in the forecast initiated in March,
169 and June, and along the South Pacific convergence zone (SPCZ) in the forecast
170 initiated in September, and December. In V2, the cold bias is mainly over the

171 central Pacific, and the magnitude of the SST bias is generally smaller than that
172 in V1. For example, in the case of the forecast initiated in March, the
173 equatorial SST bias is almost zero in V2, while for V1 the magnitude of the cold
174 SST bias reaches -1.5^{o}C (-3^{o}C) over the western (eastern) Pacific.

175 Figure 2 shows the correlation between the observed and ensemble-mean 3-
176 month averaged Sea Surface Temperature (SST) anomaly from 2 to 4 months
177 lead time initiated at the beginning of March, June, September, and December.
178 It is clear that the anomaly correlation for V2 is systematically higher than that
179 or V1 in almost all regions and seasons. For example, the V2 forecasts initiated
180 in March, have anomaly correlations over the equatorial and sub-tropical
181 Pacific, Indian Ocean, and Atlantic Ocean that are systematically higher than
182 those in V1. The same is true for the forecasts starting in June. The anomaly
183 correlation over the eastern Pacific is more than 0.8 in V2, while it is about 0.7 in
184 V1. Such an improvement is also evident in forecasts starting in September, and
185 December over the off-equatorial and subtropical Pacific, Atlantic, and Indian
186 Ocean, while there is little if any improvement over the equatorial eastern
187 Pacific.

188 The above results indicate a systematic improvement in SST forecast skill in
189 V2 compared with V1. There are, however, some exceptions, most notably the
190 equatorial western Pacific where V2 exhibits negative correlations for forecasts

initiated in June and September. This is due to fact that the simulated ENSO in V2 extends too far to the west (not shown), resulting in simulated anomalies that are of opposite sign compared to the observations over the western Pacific during ENSO.

Figure 3 shows the ENSO forecast skill in more detail, in terms of the Nino3.4 index (averaged SST anomaly over 170-120^{o}W, 5^{o}S-5^{o}N) for each start month and forecast lead time. The correlation has a clear seasonal dependency for both sets of forecasts. In V1, the forecasts starting in boreal winter or early spring exhibit relatively high skill during the early forecast lead time, however, the forecasts show relatively lower skill at long leads for the other seasons. For example, the forecasts starting in October exhibit anomaly correlations over 0.9 up to 5 month lead time, however, they show an abrupt decrease in skill after that. This is likely related to the so-called spring barrier in ENSO prediction, which is characterized by a drop in skill when the forecasts enter the boreal spring period (Chen et al. 2004). On the other hand, forecasts starting in April, exhibit correlations above 0.7 up to 9 month lead time.

The V2 forecast skill has a general behavior that is similar to that of V1, but there is clear improvement. For example, the drop in skill for forecasts starting in the boreal spring season (i.e. from February to April) does not occur in V2. In addition, there is also improvement in skill for forecasts starting in June, and

November (Fig. 2c). Even though the V2 forecasts show a slight decrease in skill after 8 months lead time for January and August, the general improvement in skill as measured by correlation is quite obvious.

The improvement in V2 forecasts is less obvious when the skill is evaluated in terms of Root Mean Square Error (RMSE). Figure 4 shows the V1 and V2 SST RMSE and the Mean Squared Skill Score (MSSS; Murphy, 1988). Here we define the MSSS as

$$\mathrm{MSSS} = \frac{\mathrm{MSE_{V1}} - \mathrm{MSE_{V2}}}{\mathrm{MSE_{V1}}}, \qquad (1)$$

where $\mathrm{MSE_{V1}}$ and $\mathrm{MSE_{V2}}$ denote the mean-squared-error (MSE) of V1 and V2, respectively. The upper limit of this value is 1 when the seasonal forecast in V2 is perfect, and a positive value indicates that the skill in V2 is better than that of the V1 in terms of MSE.

The RMSE in V1 is relatively small for forecasts initiated in August through October. In V2, the RMSE for forecasts starting in the boreal spring season is systematically smaller than that in V1. However, for forecasts starting in boreal winter the RMSE is larger in V2. As a result, the MSSS is positive (i.e. improvement in V2) for forecasts starting in boreal spring and summer, but is negative for forecasts starting in boreal fall and winter. In the case of the boreal spring and summer seasons, the improvement in V2 as measured by RMSE is

consistent with that based on the anomaly correlation, however, the decrease in skill for forecasts starting in boreal winter is only shown in the RMSE-based validation.

To summarize, the ENSO forecast skill in the two GMAO systems can be characterized as follows. 1) For forecasts starting in boreal spring and summer, V2 consistently shows better skill than V1 in terms of both the anomaly correlation and RMSE. 2) For forecasts starting in boreal fall and winter, V2 skill is similar to that of V1 in terms of correlation, but lower in terms of RMSE. In next section, we examine the causes of these differences in forecast skill.

One can wonder what causes the above apparent inconsistency between the correlation and RMSE measures of skill in forecast initiated at boreal winter season. It might be related to the differences in the simulated ENSO amplitude. The relationship between the RMSE and the correlation is as follows (Barnston, 1992).

$$\mathrm{RMSE}_{f,o} = [S_f{}^2 + S_o{}^2 - 2S_f S_o r_{f,o} + b^2]^{1/2} \qquad (2)$$

where S_f, S_o, $r_{f,o}$, b is a standard deviation of forecast, observation, correlation coefficient between forecast and observation, and bias, respectively. Even though the correlation skill is same, the different amplitude in forecasted anomaly can cause the differences in RMSE. For example, if the simulated

ENSO amplitude is larger, it can cause the larger RMSE even though the correlation skill is in similar degree. This implies that there is a systematic error in simulated ENSO amplitude in V2 initiated at boreal winter season. We will also examine this point in a next section.

4. A comparison of ENSO-related feedbacks

In order to understand the cause of the differences in forecast skill between the two systems, we first examine in Figure 5 the forecast and observed time series of the Nino3.4 index. Here we selected the forecasts starting in March, and September, which show the largest forecast-lead-month-averaged positive and negative MSSS values, respectively. Even though the general variation of the Nino3.4 index is well predicted for the March forecasts, the growth of the Nino3.4 index in V1 is often excessive. For example, during 1995, 2000, 2003, 2006, 2007, 2008, 2009, and 2010, the evolution of the Nino3.4 index in V1 is faster than that in V2 or the observations. On the other hand, for forecasts starting in September, the V2 Nino3.4 index is slightly stronger than that of V1 or the observations, though this is not as pronounced as for the March forecasts. In particular 1993/94, 1997/98, 1998/99, 2002/03, 2004/05, 2006/07, 2007/08, 2009/10 show an overshooting of Nino3.4 in V2, while a few cases have Nino3.4

stronger in V1 than in V2 (i.e. 1994/95, 2000/01 cases).

Figure 6 shows the standard deviation (STD) of MJJA SST anomalies for forecasts starting in March and September. The observed STD of the SST anomalies is about 1°C, with maximum values over the far-eastern Pacific. For the V1 forecasts starting in March, the STD of the SST anomalies is about 2.5°C over the equatorial eastern Pacific, which is more than twice the observed. For the V2 forecasts, the STD of the SST anomalies is more realistic, though the highest values extend too far to the west. In any event, the key result here is that the magnitude of the variability is excessive in V1 compared to both V2 and the observations. During the boreal winter season (when ENSO tends to peak), the STD of SST anomalies is larger than that of the other seasons (the upper panel of Figure 6). The STD of the observed SST anomalies is more than 1°C over the equatorial central-eastern Pacific. Both forecast systems simulate a too strong ENSO magnitude, with V2 having slightly larger values than V1 except over the far-eastern Pacific. For example, the simulated Nino3.4 magnitude in V1 is 1.03, while it is 1.39 in V2.

In short, it appears that to first order, deficiencies in the simulation of the amplitude of ENSO account for the differences in the forecast skill. In order to understand the causes of the excessive ENSO variability in the forecasts, we consider the Bjerknes (BJ) index (Jin et al. 2006)

$$\frac{dT}{dt} = 2I_{BJ}T + F[h] \qquad (3a),$$

where

$$2I_{BJ} = -\left(a_1 \frac{\langle \Delta u \rangle_E}{L_x} + a_2 \frac{\langle \Delta v \rangle_E}{L_y}\right) - \alpha_s + \mu_a \beta_u \langle \frac{d\bar{T}}{dx} \rangle_E + \mu_a \beta_h \langle \frac{\bar{w}}{H_1} \rangle_E a_h + \mu_a \beta_w \langle \frac{d\bar{T}}{dz} \rangle_E$$

(3b)

and

$$F = -\langle \frac{d\bar{T}}{dx} \rangle_E \beta_{uh} + \langle \frac{H(\bar{w})\bar{w}}{H_m} \rangle \qquad (3c).$$

$\langle A \rangle_E$, [A], H(A) denote a volume averaged quantity over the eastern region (the Nino3.4 region in this study), zonal mean of the equatorial Pacific basin (i.e. 120°E-90°W, 5°S-5°N in this study), and a step function whose value is 1 (0) when A is bigger (smaller) than zero, respectively. Here u, v, w, and T denote the zonal, meridional, vertical velocity, and temperature anomalies, respectively. L_x, and L_y represent the longitudinal and latitudinal length of the Nino3.4 region. a_1 and a_2 are estimated using the scale of the anomalous SSTs as in Kim and Jin (2011). The other coefficients in equation 3b, c are computed using a linear regression from the approximated balance equations, namely, $\langle Q \rangle_E = -\alpha_s \langle T \rangle_E$, $\langle H(\bar{w}) T_{sub} \rangle_E = a_h \langle h \rangle_E$, $\langle h \rangle_E - \langle h \rangle_W = \beta_h [\tau_x]$, $\langle H(\bar{w}) w \rangle_E = -\beta_w [\tau_x]$, $\langle u \rangle_E = \beta_u [\tau_x] + \beta_{uh} \langle h \rangle_w$, and $[\tau_x] = \mu_a \langle T \rangle_E$. Note that, for decomposing β_u and β_{uh}, we used multiple linear regression. Also Q, T_{sub}, h,

306 τ_x denote the net heat flux from atmosphere to ocean, the subsurface
307 temperature (50m in this study), the thermocline depth (20°C isotherm depth in
308 this study), and the zonal wind stress anomalies, respectively. The definition of
309 the western box (e.g. $\langle A \rangle_W$) is 120-180°E, 5°S-5°N.

310 The BJ index consists of five terms (i.e. right hand side of equation 3b); the
311 damping due to the mean currents (first), net heat flux (second), growth due to
312 the zonal advective feedback (third), thermocline feedback (fourth), and Ekman
313 pumping feedback (fifth). This index is a proxy for the strength of various air-
314 sea coupled feedback processes, and also a parameter to help determine
315 whether ENSO is unstable or a damped mode. Note that the zonal advective
316 feedback in the BJ index only takes into account the impact of the wind-driven
317 zonal current anomalies (β_u). We will discuss the role of zonal advection due to
318 the anomalous geostrophic current later.

319 Figure 7 shows the magnitude of each feedback process and the BJ index
320 during MJJA season for forecasts starting in March. For the observations, the
321 advection due to the mean currents and net heat flux exhibits negative values,
322 which mean that those are ENSO damping mechanisms. The magnitude of the
323 zonal advective feedback is about 0.6 °C/year, and that of the thermocline
324 feedback is slightly smaller than that. The Ekman pumping feedback is weak
325 positive. The general features are similar to those in Kim and Jin (2011), which

first applied the BJ index to climate models, though there are some differences. The biggest difference is that the strength of the thermocline feedback is stronger than that of the zonal advective feedback in Kim and Jin (2011), which is opposite to what we found here. This might be due to the fact that the eastern Pacific box is shifted 30^{o} to the west in this study to focus on the Nino3.4 region (Kang et al., 2001). Other possible reasons for the differences in the results are the difference in seasons (i.e. all seasons in Kim and Jin (2011), and MJJA in this study), and the use of different reanalysis products.

In the case of V2, the strength of each of the feedback processes is generally well simulated. The zonal advective feedback has the largest magnitude among all feedback processes, and thermal damping exhibits the minimum value, which is consistent with observations. The value of the BJ index (weak negative) is also quite similar between V2 and observations. However, the magnitude of the ENSO damping due to advection by mean current, the zonal advective feedback, and thermocline feedback is slightly stronger in V2 than for the observations. The differences are, however, less than 0.5^{o}C/year for all feedback processes.

On the other hand, the BJ index in the V1 forecasts is too strong, which is consistent with stronger STD of SST shown in Fig. 6. The BJ index is more than 1^{o}C/year, which is significantly larger than for V2 or observations. This is due to

the excessive zonal advection feedback, thermocline feedback, and Ekman pumping feedback. The weak thermal damping also plays some role. Among them, zonal advective feedback exhibits the biggest difference with respect to the observations, suggesting that may be the main factor in producing the stronger ENSO magnitude in V1.

We next investigate the reasons for the stronger zonal advective feedback in V1. The zonal advection feedback is determined by three factors; air-sea coupling strength μ_a, the sensitivity of ocean current to the surface wind forcing β_u, and mean zonal temperature gradient $\langle\frac{d\bar{T}}{dx}\rangle_E$. Once a positive El Nino SST anomaly is produced, it induces anomalous equatorial westerlies, which in turn generate westerly currents. The current advects the mean temperature over the western Pacific to the eastern Pacific to induce additional positive El Nino SST anomalies. Checking the above three terms, we found that the sensitivity of the ocean current to the surface wind forcing (i.e. β_u) is too strong in the forecasts.

Figure 8 shows the linear regression coefficients of surface-layer zonal current (surface to 50m) onto the equatorial Pacific-mean zonal wind stress anomalies during MJJA season. As mentioned earlier, the contribution of the geostrophic current is excluded in this calculation. For the observations, the response of the surface-layer zonal current is between 5 and 10 m/s/N/m^2 over

366 the equatorial Pacific, comparable to the results of Jin et al. (2006). In contrast,
367 the responses in both forecasts are substantially stronger than the observed.
368 This is especially true for V1, for which the response of the ocean zonal current
369 to the zonal wind stress is about 40 m/s/N/m^2, while for V2 it is about 20-30
370 m/s/N/m^2. Over the Nino3.4 region, the observational value is 5.8 m/s/N/m^2,
371 while for V1, and V2 it is 22.5 m/s/N/m^2, and 15.1 m/s/N/m^2, respectively. This
372 shows clearly that the excessive zonal advective feedback in the forecasts is due
373 to the unrealistic response of the surface-layer oceanic current to the zonal wind
374 stress forcing.

375 Figure 9 shows the strength of each of the air-sea coupled processes and the
376 BJ index during NDJF for forecasts starting in September. The BJ index based on
377 the observations shows a negative value (i.e. -0.46). The BJ index for V1 is
378 slightly larger (-0.23). On the other hand, V2 has a positive value of the index,
379 which is consistent with the excessive ENSO variability in the forecasts. The
380 zonal advective feedback appears to be the main contributor to the excessive BJ
381 index in V2. While also stronger than observed in V1, zonal advective
382 feedback is not as excessive as that in V2. This is opposite to the results for the
383 March forecast where V1 shows excessive zonal advective feedback strength.

384 We next assess the causes of the change in the strength of the zonal
385 advective feedback between two sets of forecast initiated at March and

September. We found that the sensitivity of ocean current to the surface wind forcing β_u, and mean zonal temperature gradient $\langle\frac{d\bar{T}}{dx}\rangle_E$ are similar between two sets of forecasts. However, there is a large difference in the air-sea coupling strength (μ_a). In the observations, the air-sea coupling strength (defined as the linear regression of zonal wind stress anomalies averaged over the equatorial Pacific (120-90°W, 5°S-5°N) onto the Nino3.4 SST anomalies during NDJF season) is 0.0047 N/m²/°C. That in V2 is quite similar to the observed (0.0045 N/m²/°C), however, in V1 the air-sea coupling strength is only half that (0.0020 N/m²/°C), indicating that the response of equatorial wind stress anomalies to El Nino SST forcing is significantly weaker in V1. As a result, for the V1 September forecasts, the weak air-sea coupling strength mitigates the excessive zonal advective feedback due to the strong sensitivity of the oceanic current (β_u). On the other hand, the excessive sensitivity of the oceanic current in the V2 forecasts is directly impacted by the too strong zonal advective feedback.

5. The impact of the recharge/discharge process

In a previous section, we utilized the BJ index to investigate ENSO characteristic in forecasts and observation. This, however, does not take into account the impact of the geostrophic current associated with the

405 recharge/discharge of equatorial heat content, which is particularly important
406 for determining the ENSO period (Jin et al. 2006). As such, the zonal-mean heat
407 content and related geostrophic zonal current are important factors for
408 determining the growth and demise of ENSO, and are likely to be particularly
409 important during the ENSO peak season.

410 To examine how the geostrophic current influences the phase transition or
411 demise of the ENSO, Figure 10 shows the composite of the thermocline depth
412 anomaly and surface-layer zonal currents in observations, V1, and V2 during
413 the El Nino events. We selected 5 El Nino cases (i.e. 1994/95, 1997/98, 2002/03,
414 2006/07, and 2009/10) for the composite analysis. Note that we focus on the
415 forecasts starting in September since we did not find any systematic differences
416 between the forecasts starting earlier in the year (not shown). For the
417 observations, there is maximum over the equatorial eastern Pacific with
418 negative values over the western Pacific during November. In addition, off-
419 equator around 5^{o}N, the negative thermocline depth anomaly is clearly evident.
420 This induces an anomalous negative meridional gradient in the height, which is
421 associated with an anomalous westerly current through the geostrophic balance.
422 There is also a weak easterly current over the equatorial central Pacific, which
423 becomes stronger beginning in December, while the off-equatorial westerly
424 current disappears. The change in sign of the equatorial zonal current anomaly

425 from westerly to easterly in December acts as a brake on the evolution of the El
426 Nino event. The equatorial easterly current is directly linked to the spatial
427 pattern of the thermocline depth anomaly (a minimum over the equator) which
428 results from the discharge of equatorial heat content during the El Nino due to
429 divergent meridional currents (Jin, 1997).

430 In V1, this discharge process is slower than observed, however, the
431 thermocline depth anomaly does exhibit a minimum at the equator starting in
432 January. In addition, the positive thermocline depth anomaly is shifted from the
433 equator in November to off the equator at February, indicating that the
434 discharge of equatorial heat content is simulated to some extent in V1. On the
435 other hand, this discharge process is not effective in V2. The positive
436 thermocline depth anomaly still has a maximum over the equator, and the off-
437 equatorial negative anomaly continues into February. This implies that the
438 discharge process in V2 is much slower than what occurs in V1 or the
439 observations. As a result, the westerly current in V2 is maintained up to January,
440 and the magnitude of the easterly current is systematically weaker than that in
441 either V1 or observation. This results in excessive warm temperature advection,
442 which is not evident in V1 or the observations, and El Nino SST anomalies
443 continue to grow even after it starts to decay in the observations and V1. This
444 appears to be one of the mechanisms contributing to the overshoot of ENSO in

V2 as shown in Fig. 5.

The discharge process is mainly driven by the equatorial divergent meridional flow over the thermocline layer (Jin, 1997), so we would expect that the V2 equatorial meridional current would be weak. Figure 11 shows the El Nino composite of the meridional current averaged from surface to 200m over the central Pacific (160°E-80°W). In V1, the magnitude of divergent flow is less than 1 cm/s, while the observational value is over 1.2 cm/s. In addition, there is northward current south of the equator, which is related to the mass recharge at the equator. In V2, the magnitude of the divergent flow is similar to that in V1 poleward of 5°N, but it is systematically weaker between 0-5°N. This is consistent with Fig. 10 in that the discharge of the equatorial heat content is not effective in V2, and this is responsible for the persistent positive equatorial thermocline depth anomaly and westerly current.

In order to understand why the equatorial meridional current is systematically weaker in V2 we examine the following Sverdrup balance equation:

$$\rho v_s H = \frac{-1}{\beta}\frac{\partial \tau_x}{\partial y}, \quad (4)$$

where ρ, v_s, H denote the water density, meridional current for Sverdrup transport, and the mean thermocline depth, respectively. Once there are

westerlies at the equator, the meridional gradient of zonal wind stress is negative north of equator, which leads to equatorial divergent flows. To check whether this relationship holds in the observations and forecasts, we show in Figure 12 the composite of the zonal wind stress over the central Pacific (160°E-80°W). For the observations, the peak of the westerly wind forcing is at the equator, and so the meridional gradient of the zonal wind stress is negative north of the equator. On the other hand, the positive meridional gradient of zonal wind stress south of the equator is quite weak, consistent with the hemispheric asymmetric feature in divergent flow (Kug et al. 2003).

In V1, the peak of westerly wind stress is at 2°S, and so the northward mass transport occurs north of 2°S, which is consistent with Fig. 11b that the northward flow is south of the equator, consistent with the Sverdrup. In V2, the peak in the westerly wind stress occurs north of the equator (i.e. 2°N), so that the sign of the meridional gradient of the zonal wind stress is positive between 0-2°N, which is opposite to that in V1 or observation. The associated weak divergent flow at the equator, suggests that the unrealistic atmospheric response during El Nino might be responsible for the slower ENSO demise in V2.

Figure 13 shows the El Nino composite of precipitation and zonal wind stress anomaly in the observations and forecasts. The observed precipitation

anomaly during El Nino events shows maximum values over the central Pacific. There are two peaks in the precipitation anomaly; one south of the equator between 5-0^{o}S, and the other between 0-5^{o}N. The northern part of the precipitation anomaly is elongated over the region where the climatological precipitation is relatively large (i.e. Intertropical Convergence Zone, ITCZ). In V1, the overall pattern is well simulated, however, the precipitation anomaly is shifted to the south. On the other hand, the anomalous precipitation in V2 is confined to the northern hemisphere, lacking the maximum south of the equator, though that to the north along the ITCZ is as strong as observed.

The spatial pattern of the zonal wind stress anomaly is dynamically linked to the precipitation anomaly (the lower panel of Figure 13). For the observations, the peak in the zonal wind stress is over the central Pacific south of the equator where the precipitation anomaly is a maximum, (Harrison and Vecchi, 1999). As the anomalous precipitation extends to the east along the ITCZ, the north-eastern edge of the zonal wind stress extends slightly to the east. In V1, the zonal wind stress anomaly and precipitation anomaly are both confined to be south of the equator. In V2, the center of zonal wind stress is slightly shifted to the north compared to the observed and V1, even though it still lies south of the equator. Another aspect of the V2 stress is that the off-equatorial westerly stress along the ITCZ is stretched too far to the east. This additional westerly stress

along the ITCZ contributes to the unrealistic peak of zonal wind stress north of the equator. This is consistent with the precipitation anomaly composite which is confined to be north of the equator.

The unrealistic extension of the zonal wind stress along the ITCZ, suggests a possible bias in the precipitation over this region. In particular, a wet climatology provides favorable conditions for stronger anomalous convection (Watanabe et al. 2011; Kim et al. 2011; Ham and Kug, 2012), leading to enhanced surface winds. Figure 14 shows the climatological precipitation fields for the observations and the model simulations. V2 clearly has a wet bias along the ITCZ and that is strongest over the central Pacific between 180-120^{o}W – the region where the ENSO-related convection is elongated and the westerly wind stress is unrealistic. This suggests that the wet bias over the central Pacific ITCZ might provide the background for inducing the excessive precipitation anomalies and the related anomalous westerlies along the ITCZ.

6. Summary and discussions

In this study, the forecast skills of two versions of GMAO seasonal prediction system are evaluated. The more recent version of the forecast system with the GEOS-5 model (V2) exhibits overall better skill than the previous

523 version based on the NSIPP model (V1). The correlation skill in V2 is
524 systematically higher in most regions except for the equatorial western Pacific.
525 This improvement is robust especially for forecasts starting early in the year. On
526 the other hand, when the forecast skill is measured by RMSE, the skill of the
527 Nino3.4 index is slightly worse in V2 for forecasts initiated during the boreal
528 winter season. We found that the forecast skill degrades relatively fast because
529 the simulated ENSO is generally too strong. In particular, for forecasts starting
530 early in the year, V1 tends to simulate too strong ENSO amplitudes (so V1 skill
531 is less than that of V2), while for forecasts starting in boreal winter there is some
532 overshooting of the ENSO anomaly in V2, and the skill in V2 is slightly worse
533 than that in V1.

534 By utilizing the BJ index from Jin et al. (2006), we examined the reasons for
535 why the ENSO magnitude in V1 (V2) is excessive in the forecast starting early
536 (late) in the year. For the forecasts starting in March, it was shown that the
537 positive ENSO feedbacks (the zonal advective feedback, thermocline feedback,
538 and Ekman feedback) are excessive in V1. This together with weak thermal
539 damping explains the excessive ENSO magnitude. Among the above factors,
540 the magnitude of the zonal advective feedback exhibits the largest differences
541 with the observations. This difference occurs primarily because the response of

542 the wind-driven current to the wind forcing is too sensitive in V1, since the
543 other processes are generally well simulated. This basic sensitivity is also
544 excessive in V2, however, less so compared with V1.

545 For the forecast starting late in the year, the ENSO amplitude is stronger
546 than the observed in both versions, but more excessive in V2. This is again due
547 to a strong oceanic sensitivity to the wind forcing. However, in V1 the air-sea
548 coupling strength is only half of the observed, which mitigates the excessive
549 oceanic sensitivity. Therefore, the overall strength of the zonal advective
550 feedback in V1 is similar degree with the observed. On the other hand, the
551 excessive sensitivity of the oceanic current in the V2 forecasts is directly
552 impacted by the too strong zonal advective feedback.

553 In addition to the wind-driven zonal current, which is taken into account in
554 the BJ index, it is found that geostrophic currents are also important in
555 determining the ENSO characteristics in the forecasts during its peak phase. For
556 the V2 forecasts that are initiated during boreal winter, there is a too slow phase
557 transition of El Nino due to the weak discharge of equatorial WWV. This delays
558 the transition of equatorial current from westerly to easterly, and contributes to
559 the overshooting of the ENSO in V2. This weak discharge of the equatorial heat

560 content in V2 is related to an erroneous spatial pattern of the anomalous zonal
561 wind stress. That is, the ENSO-related zonal wind stress in V2 shows unrealistic
562 peak along the ITCZ, while that in V1 and the observation show maximum at
563 the south of the equator. This unrealistic peak in ENSO-related zonal wind
564 stress is linked to the confinement of ENSO-related precipitation anomaly at the
565 north of the equator, which is possibly due to the excessive climatological
566 precipitation in the ITCZ.

567 This study focused on the physical mechanisms which control the ENSO
568 prediction skill in two substantially different forecast systems. The hope is that
569 this can provide some guidance to model development aimed at improving
570 forecast skill on seasonal and longer time scales. On the other hand, it must be
571 acknowledged that a large portion of the forecast skill is also controlled by the
572 quality of the initial conditions (Rosati et al. 1997; Behringer et al. 1998; Tang
573 and Kleeman 2002; Rogel et al. 2005). Since the initial conditions between two
574 GMAO seasonal forecast systems is different by using different observations
575 and perturbing method even though the initialization method is similar, we
576 believe that differences documented here are also affected by the differences in
577 initial conditions.

578

579 **References**

580 Adler RF, and Coauthors (2003) The version 2 global precipitation climatology
581 project (GPCP) monthly precipitation analysis (1979-present) J.
582 Hydrometeor, 4: 1147–1167.
583 Bacmeister J, Pegion PJ, Schubert SD, Suarez MJ (2000) Atlas of seasonal means
584 simulated by the NSIPP 1 atmospheric GCM. NASA Tech. Memo. 2000-
585 104606, Vol. 17, 194 pp.
586 Balmaseda MA, Anderson D (2009) Impact of initialization strategies and
587 observations on seasonal forecast skill. Geophys. Res. Lett., 36: L01701,
588 doi:10.1029/2008GL035561.
589 Barnston AG (1992) Correspondence among the correlation, RMSE, and Heidke
590 forecast verification measures; Refinement of the Heidke Score. Weather and
591 Forecasting, 7: 699-709.
592 Behringer DW, Ming J, Ants L (1998) An Improved Coupled Model for ENSO
593 Prediction and Implications for Ocean Initialization. Part I: The Ocean Data
594 Assimilation System. Mon. Wea. Rev., 126: 1013–1021.
595 Behringer DW, Xue Y (2004) Evaluation of the global ocean data assimilation
596 system at NCEP: The Pacific Ocean. Preprints, Eighth Symp. on Integrated
597 Observing and Assimilation Systems for Atmosphere, Ocean and Land
598 Surface, Seattle, WA, Amer. Meteor. Soc., 11–15. [Available online at
599 http://ams.confex.com/ams/84Annual/webprogram/Paper70720.html.]
600 Chen D, Cane MA, Kaplan A, Zebiak SE, Huang DJ (2004) Predictability of El
601 Nino over the past 148 years. Nature, 428: 733–736.
602 Dee D, and Coauthors (2011) The ERA-Interim reanalysis: Configuration and
603 performance of the data assimilation system. Quart. J. Roy. Meteor. Soc., 137:
604 553–597.
605 Griffies SM, and Coauthors (2005) Formulation of an ocean model for global
606 climate simulations. Ocean Science, 1: 45-79.
607 Ham Y-G, Kug J-S, Kang I-S (2009) Optimal initial perturbations for El Nino
608 ensemble prediction with Ensemble Kalman Filter, Clim. Dyn. 33: 959–973,
609 10.1007/s00382-009-0582-z.
610 Ham Y-G, Kang I-S, Kim D, Kug J-S (2012a) El-Nino Southern Oscillation
611 Simulated and Predicted in SNU Coupled GCMs, Clim. Dyn., 38: 2227-2242,

612 10.1007/s00382-011-1171-5.
613 Ham Y-G, Kang I-S, Kug J-S (2012b) Coupled Bred Vectors in the Tropical
614 Pacific and Their Application to ENSO prediction, Prog. Oceanogr., 105: 90-
615 101, 10.1016/j.pocean.2012.04.005.
616 Ham Y–G, Schubert S, Chang Y (2012c) Optimal Initial Perturbations for
617 Ensemble Prediction of the Madden-Julian Oscillation during Boreal Winter,
618 J. Clim., 25: 4932-4945, 10.1175/JCLI-D-11-00344.1.
619 Ham Y–G, Rienecker MM, Schubert S, Marshak J, Yeh S-W, Yang S-C (2012d)
620 The decadal Modulation of coupled bred vectors, Geophy. Res. Lett., 37:
621 L20712, 10.1029/2012GL053719.
622 Ham Y-G, Kug J-S (2012) How well do current climate models simulate two-
623 types of El Nino?. Climate Dynamics 39: 383-398, 10.1007/s00382-011-1157-3.
624 Jin F-F (1997) An equatorial recharge paradigm for ENSO. Part I: Conceptual
625 model, J. Atmos. Sci., 54: 811–829.
626 Jin F-F, Kim ST, Bejarano L (2006) A coupled-stability index for ENSO. Geophys.
627 Res. Lett., 33: L23708, doi:10.1029/2006GL027221.
628 Kang I-S, An S-I, Jin F-F (2001) A Systematic Approximation of the SST
629 Anomaly Equation for ENSO, J. Meteor. Soc. Japan. 79: 1-10.
630 Keppenne CL, Rienecker MM, Jacob JP, Kovach R (2008) Error covariance
631 modeling in the GMAO ocean ensemble Kalman filter. Mon. Weather Rev.,
632 136: 2964–2982.
633 Kim S, Jin FF (2011) An enso stability analysis. part ii: results from the twentieth
634 and twenty-first century simulations of the cmip3 models. Clim Dyn
635 36:1609–1627.
636 Kim D, Jang Y-S, Kim D-H, Kim Y-H, Watanabe M, Jin F-F, Kug J-S (2011) El
637 Niño–Southern Oscillation sensitivity to cumulus entrainment in a coupled
638 general circulation model. J. Geophys. Res., 116: D22112,
639 doi:10.1029/2011JD016526.
640 Koster R, Suarez M (1992) Modeling the land surface boundary in climate
641 models as a composite of independent vegetation stands. J. Geophys. Res.,
642 97: 2697–2715.
643 Kug J-S, Kang I-S, An S-I (2003) Symmetric and anti-symmetric mass exchanges
644 between the equatorial and off-equatorial Pacific associated with ENSO, J.
645 Geophy. Res. -Oceans. 108: C8, 3284.
646 Kug J-S, Ham Y-G, Lee E-J, Kang I-S (2011) Empirical singular vector method
647 for ensemble El Nino-Southern Oscillation Prediction with a coupled

general circulation model, J. Geophy. Res., 116: C08029, 10.1029/2010JC006851.

Lin S-J (2004) A vertically Lagrangian finite-volume dynamical core for global models. Mon. Wea. Rev., 132: 2293–2307.

Luo J-J, Masson S, Roeckner E, Madec G, Yamagata T (2005) Reducing climatology bias in an ocean–atmosphere CGCM with improved coupling physics. J. Clim., 18: 2344–2360.

Molod, A., L. Takacs, M. Suarez, J. Bacmeister, I.-S. Song, and A. Eichmann, 2012. The GEOS-5 Atmospheric General Circulation Model: Mean Climate and Development from MERRA to Fortuna**.** *Technical Report Series on Global Modeling and Data Assimilation*, 28

Molteni F, and Coauthors (2011) The new ECMWF seasonal forecast system (System 4). ECMWF Technical Memorandum 656.

Moorthi S, Suarez MJ (1992) Relaxed Arakawa–Schubert:A parameterization of moist convection for general circulation models. Mon. Wea. Rev., 120: 978–1002.

Murphy JM (1988) The impact of ensemble forecasts on predictability, Q. J. R. Meteorol. Soc., 114: 463-493.

Palmer TN, and Coauthors (2004) Development of a European Multimodel Ensemble System for Seasonal-to-Interannual Prediction (DEMETER)., Bull. Amer. Meteor. Soc., 85: 853–872.

Rienecker MM, and Coauthors (2007) The GEOS-5 data assimilation system—Documentation of versions 5.0.1, 5.1.0, and 5.2.0. NASA/TM-2007-104606, Vol. 27.

Rienecker MM, and Coauthors (2011) MERRA: NASA's Modern-Era Retrospective Analysis for Research and Applications. J. Climate, 24: 3624–3648.

Rosati A, Miyakoda K, Gudgel R (1997) The impact of ocean initial conditions on ENSO forecasting with a coupled model. Mon. Wea. Rev.,125: 754–772.

Rogel P, Weaver AT, Daget N, Ricci S, Machu E (2005) Ensembles of global ocean analyses for seasonal climate prediction: Impact of temperature assimilation. Tellus A, 57: 375–386.

Saha S, and Coauthors (2006) The NCEP Climate Forecast System. J. Clim., 19: 3483 – 3517.

Schopf P, Loughe A (1995) A reduced-gravity isopycnal ocean model: Hindcasts of El Nino. Mon. Wea. Rev., 123: 2839–2863.

684 Tang Y, Kleeman R (2002) A new strategy for assimilating SST data for ENSO
685 predictions, Geophys. Res. Lett., 29: 1841, DOI: 10.1029/2002GL014860.
686 Vernieres, G., and co-authors, 2013: The GEOS-ODAS, description and
687 evaluation. NASA Technical Memorandum (in preparation).
688 Wang G, Kleeman R, Smith N, Tseitkin F (2002) The BMRC coupled general
689 circulation model ENSO forecast system. Mon. Wea. Rev., 130: 975–991.
690 Wang B, and Coauthors (2009) Advance and prospectus of seasonal prediction:
691 assessment of the APCC/CliPAS 14-model ensemble retrospective seasonal
692 prediction (1980–2004). Clim Dyn, 33, doi:10.1007/s00382-008-0460-0.
693 Watanabe M, Chikira M, Imada Y, Kimoto M (2011) Convective control of
694 ENSO simulated in MIROC. J Clim 24:543–562
695 Yang S-C, Cai M., Kalnay E, Rienecker M, Yuan G, Toth Z (2006) ENSO bred
696 vectors in coupled ocean-atmosphere general circulation models. J. Clim 19:
697 1422-1436.
698 Yang S-C, Kalnay E, Cai M, Rienecker MM (2008) Bred vectors and tropical
699 pacific forecast errors in the NASA coupled general circulation model. Mon.
700 Wea. Rev., 136: 1305-1326.
701 Yin Y, Alves O, Oke PR (2011) An ensemble ocean data assimilation system for
702 seasonal prediction. Mon. Wea. Rev., 139: 786–808.
703 Yoo J-H, Kang I-S (2005) Theoretical examination of a multi-model composite
704 for seasonal prediction. Geophys Res Lett, 32: L15711.
705 doi:10.1029/2005GL023513
706 Yuan X, Wood EF, Luo LF, Pan M (2011) A first look at Climate Forecast System
707 version 2 (CFSv2) for hydrological seasonal prediction. Geophys Res Lett, 38:
708 L13402. doi:10.1029/2011GL047792.
709 Zhang S, Harrison MJ, Rosati A, Wittenberg A (2007) System design and
710 evaluation of coupled ensemble data assimilation for global oceanic climate
711 studies. Mon. Wea. Rev., 135: 3541–3564.
712

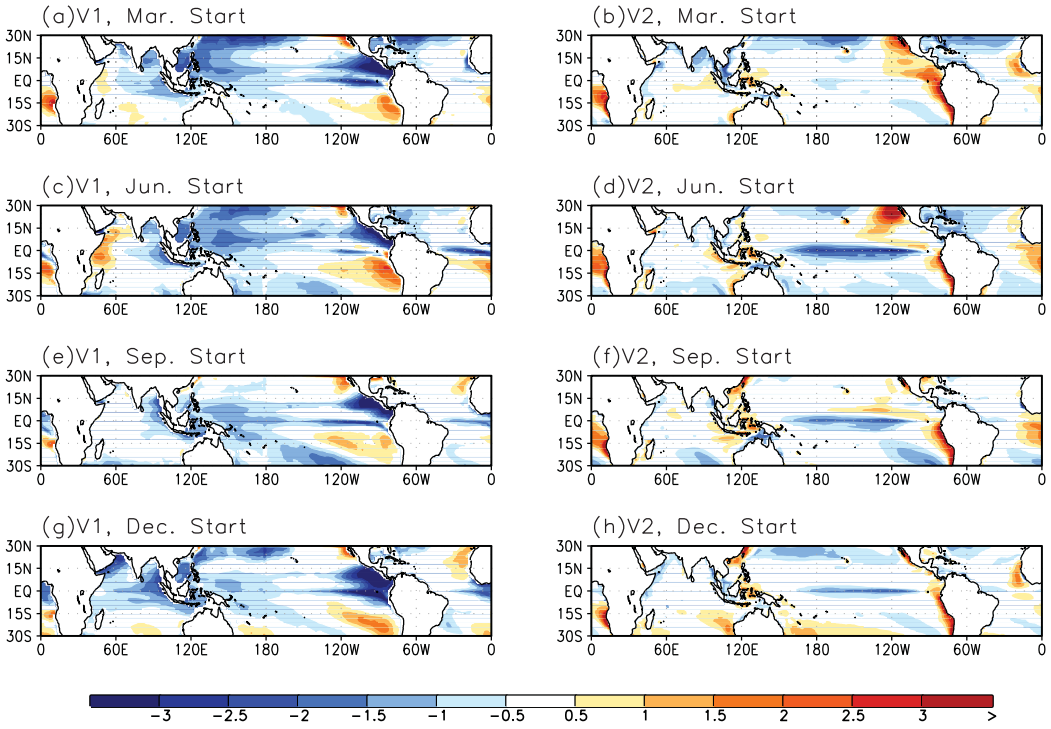

Figure 1. The climatological bias in 3-month averaged SST from 2 to 4 month lead initiated at March, June, September, and December 1st in V1 (left panels), and V2 (right panels).

720

721

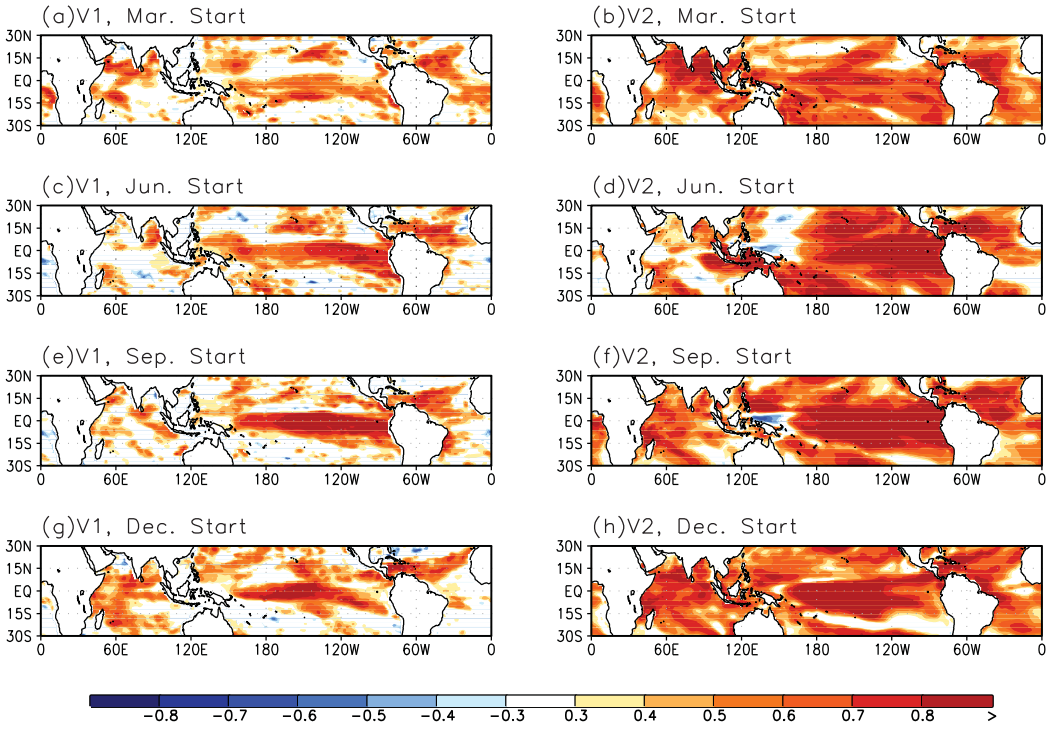

722

723 Figure 2. Same as Fig. 1, but for correlation skill of SST anomaly between the

724 observed and the predicted.

725

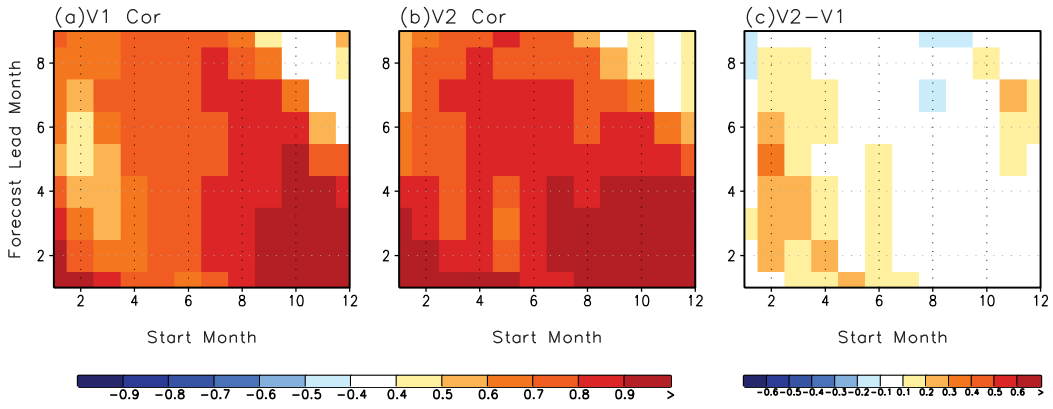

Figure 3. The correlation skill of Nino3.4 index with respect to the start month (x-axis) and forecast lead month (y-axis) in (a) V1, and (b) V2. The panel (c) shows the difference of the correlation skill (i.e. V2-V1).

734

735

736

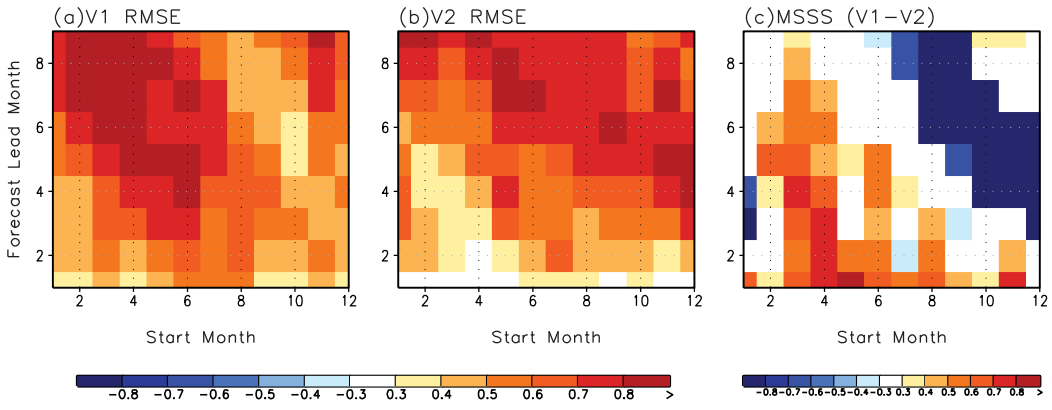

737

738 Figure 4. Same as Fig. 3, but for RMSE. The panel (c) shows the MSSS score.

739

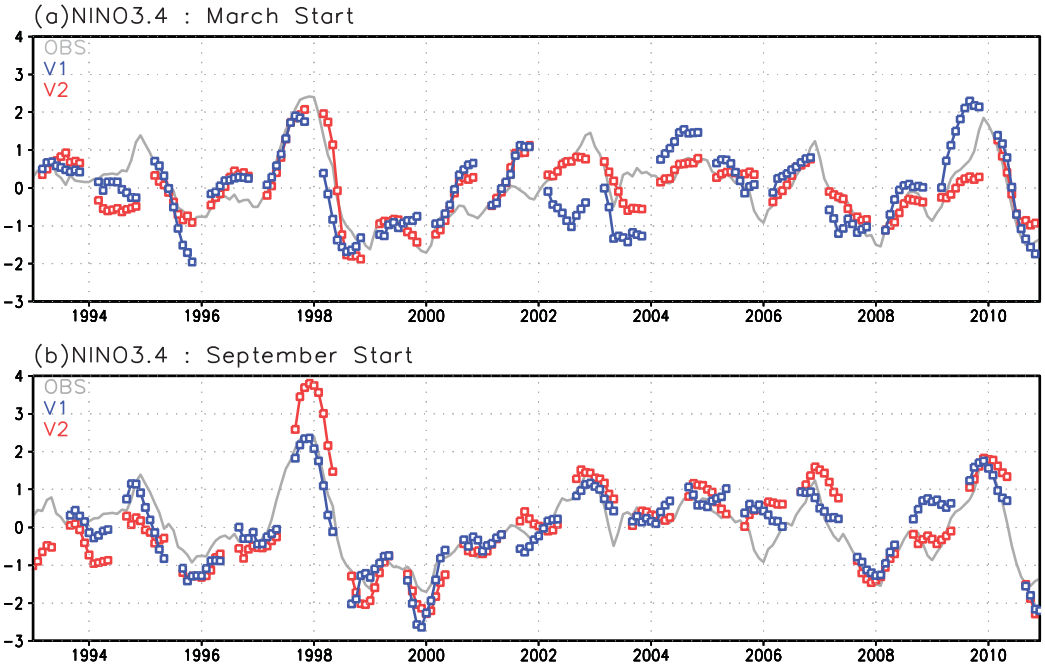

Figure 5. Time series of predicted ensemble-mean Nino3.4 index in V1 (blue), V2 (red) in the forecast starting at (a) March, and (b) September 1st . The observed Nino3.4 index is shown as a grey line.

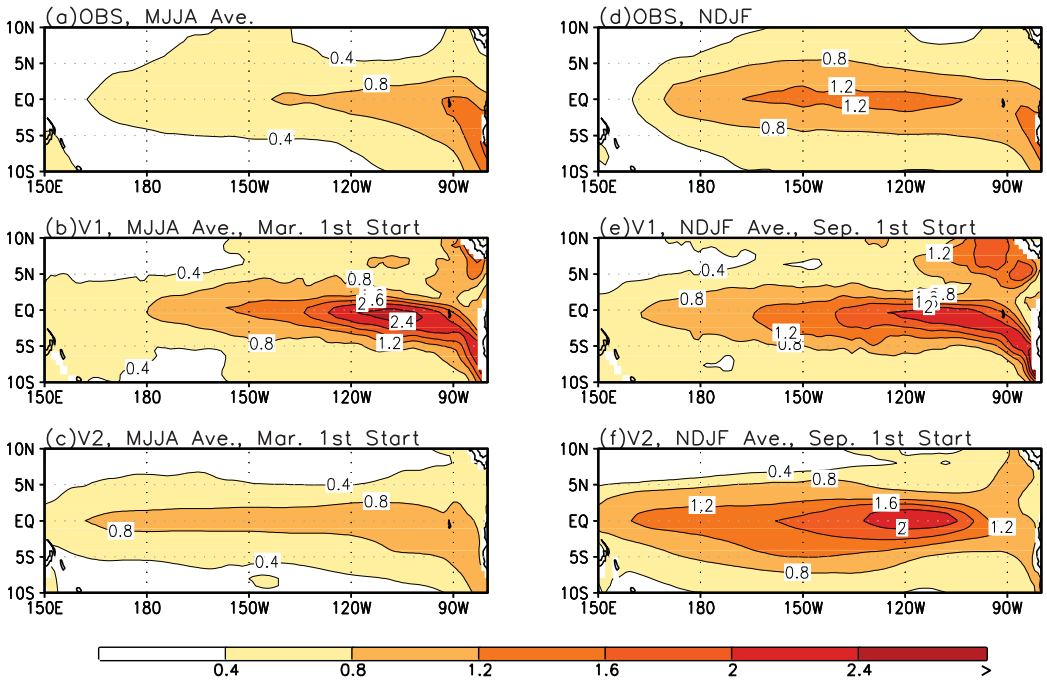

Figure 6. The left panel shows the standard deviation (STD) of SST anomaly in (a) observation, (b) V1, and (c) V2 forecast for MJJA season. We utilize the forecast starting at March 1st. The right panel is the STD of SST anomaly during NDJF season using the forecast starting at September 1st.

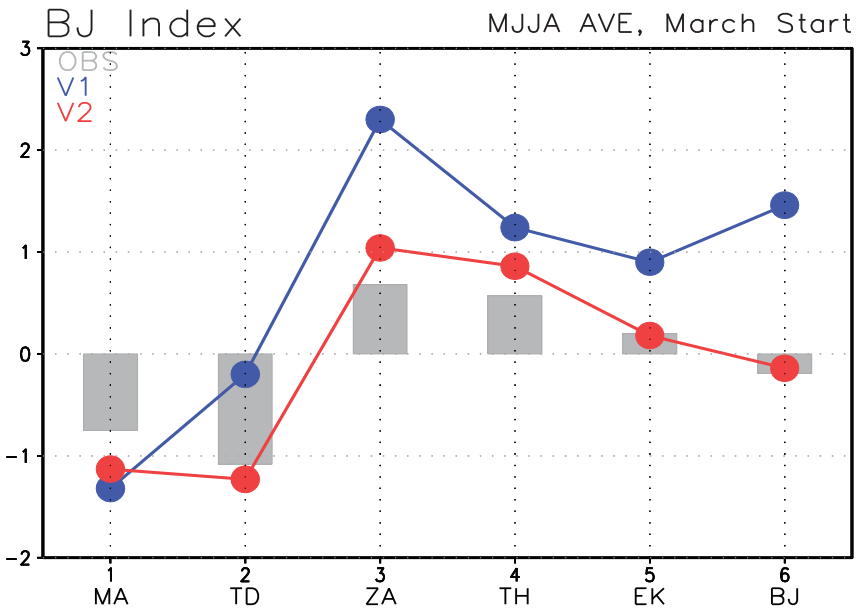

Figure 7. The strength of the damping due to the mean currents (1, denoted as MA), net heat flux (2, denoted as TD), and growth due to the zonal advective feedback (3, denoted as ZA), thermocline feedback (4, denoted as TH), and Ekman pumping feedback (5, denoted EK), and BJ index (6, denoted as BJ) during MJJA in observation (grey bar), V1 (blue line), and V2 (red line). We utilize the forecast starting at March 1st.

765

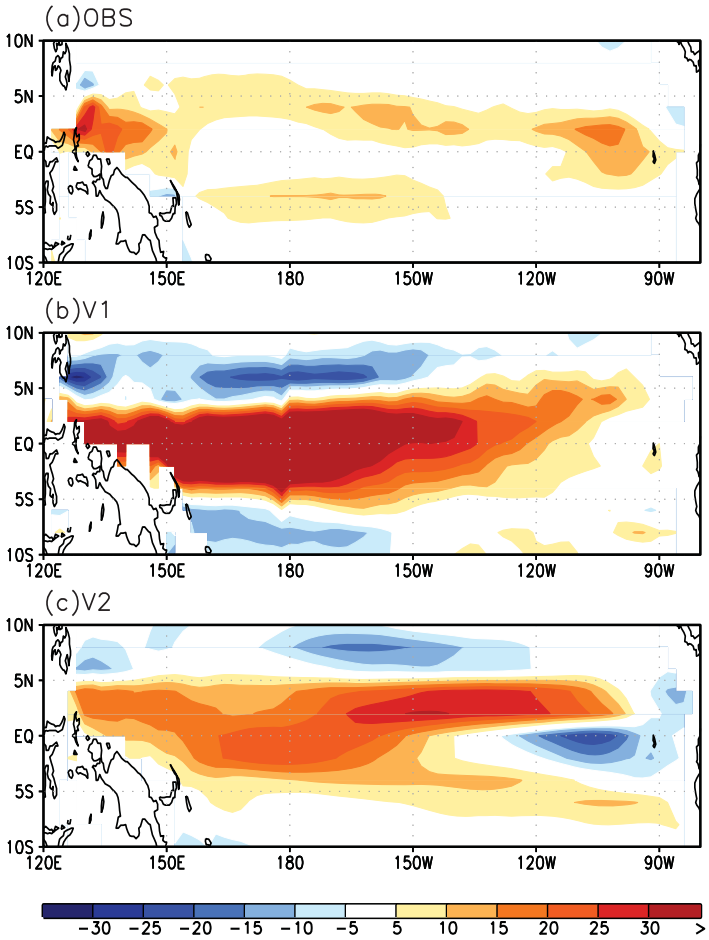

766

767 Figure 8. The linear regression of oceanic zonal current at the surface-layer

768 (0-50m average) to the equatorial Pacific-mean (i.e. 120°E-90°W, 5°S-5°N) zonal

769 wind stress anomaly in (a) observation, (b) V1, and (c) V2 during MJJA season.

770 We utilize the forecast starting at March 1st.

771

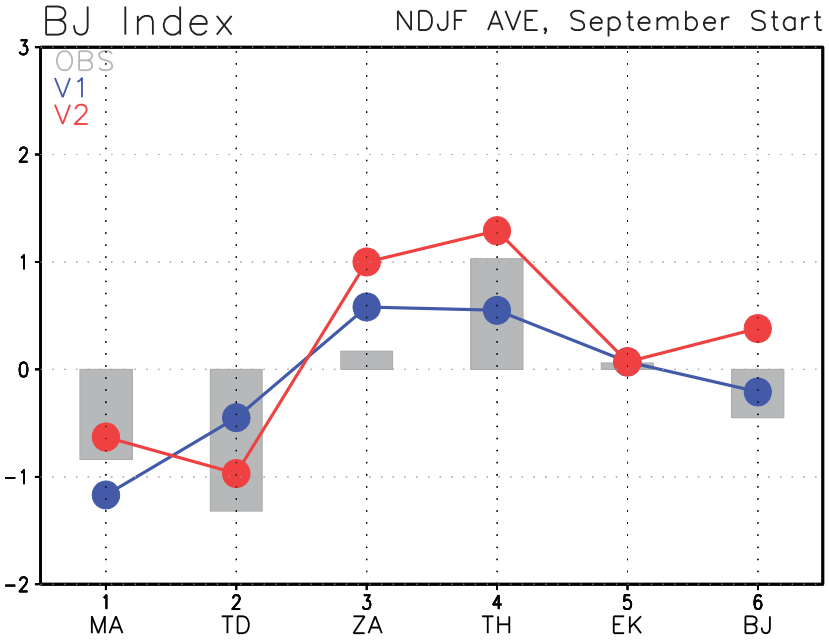

Figure 9. The strength of the damping due to the mean currents (1, denoted as MA), net heat flux (2, denoted as TD), and growth due to the zonal advective feedback (3, denoted as ZA), thermocline feedback (4, denoted as TH), and Ekman pumping feedback (5, denoted EK), and BJ index (6, denoted as BJ) during NDJF in observation (grey bar), V1 (blue line), and V2 (red line). We utilize the forecast starting at September 1st.

783

784

785

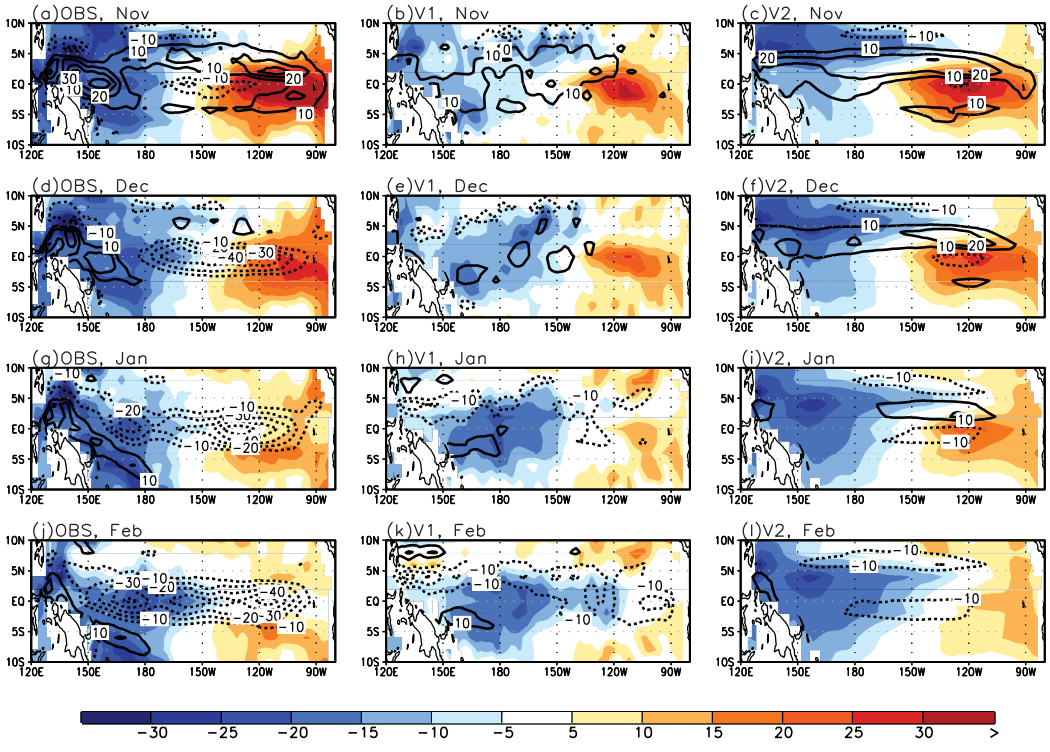

786

787 Figure 10. The El Nino composite of the thermocline depth anomaly

788 (shading) and surface-layer zonal currents (contour) in observations (left panel),

789 V1 (mid-panel), and V2 (right panel) from November to subsequent February.

790 We utilize the forecast starting at September 1st.

791

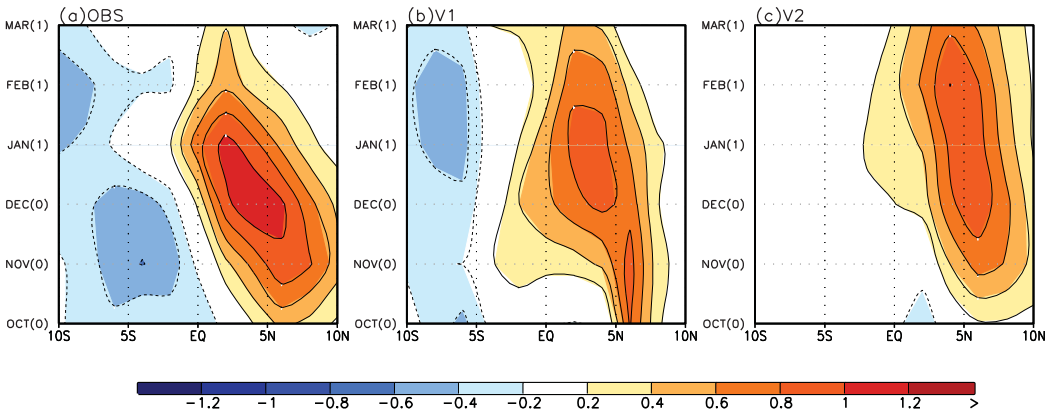

Figure 11. Time-latitude section of the meridional current averaged from surface to 200m over the central Pacific (160°E-80°W) in (a) observation, (b) V1, and (c) V2 during the El Nino event. We utilize the forecast starting at September 1st.

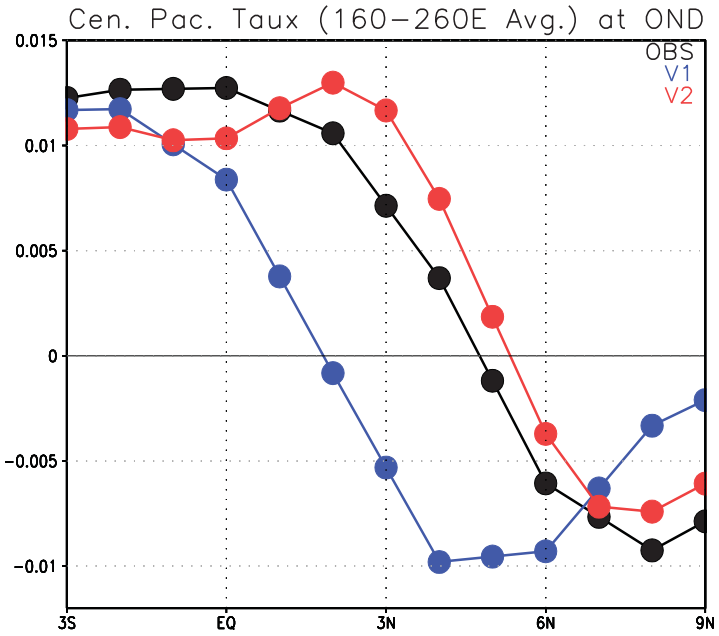

Figure 12. The El Nino composite of the zonal wind stress over the central Pacific (160°E-80°W) in observation (black), V1 (blue), and V2 (red) during OND season.

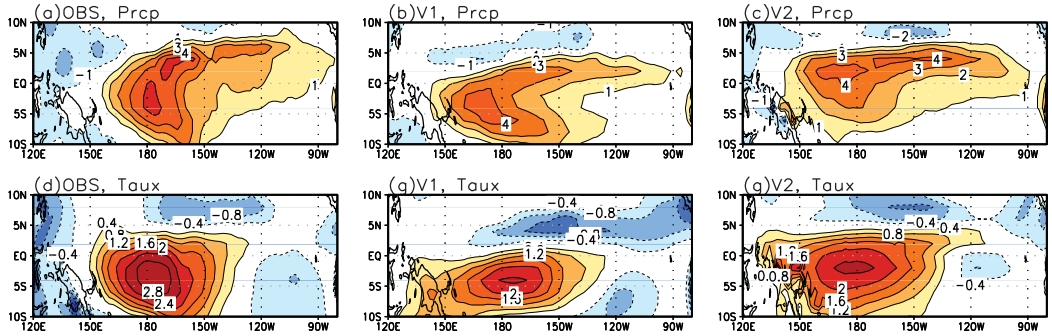

Figure 13. The El Nino composite of precipitation (upper panels) and zonal wind stress anomaly (lower panels) in observation and forecasts during OND season.

819

820

821

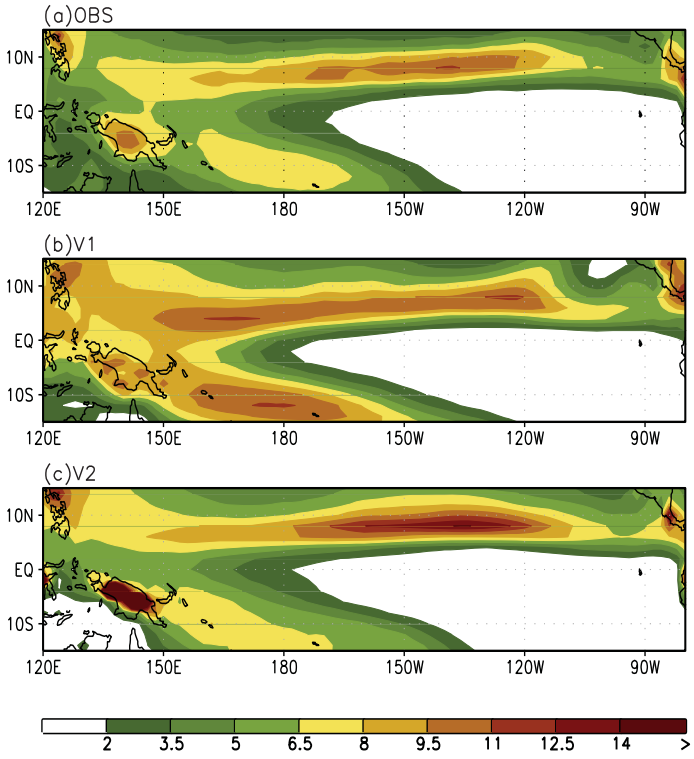

822

823 Figure 14. The climatological precipitation fields in (a) observation, (b) V1,

824 and (c) V2 during OND season.

825